Crustal geometry of the northeastern Gulf of Aden passive margin : localization of the deformation inferred from receiver function analysis

Christel Tiberi, Sylvie Leroy, Elia d'Acremont, Nicolas Bellahsen, C. Ebinger, A. Al-Lazki, Agnès Pointu

To cite this version:

Christel Tiberi, Sylvie Leroy, Elia d'Acremont, Nicolas Bellahsen, C. Ebinger, et al.. Crustal geometry of the northeastern Gulf of Aden passive margin : localization of the deformation inferred from receiver function analysis. Geophysical Journal International, 2007, 168, pp.1247-1260. 10.1111/j.1365-246X.2006.03294.x . hal-00137030

HAL Id: hal-00137030
https://hal.science/hal-00137030

Submitted on 14 Oct 2021

Geophys. J. Int. (2007) **168,** 1247–1260 doi: 10.1111/j.1365-246X.2006.03294.x

Crustal geometry of the northeastern Gulf of Aden passive margin: localization of the deformation inferred from receiver function analysis

C. Tiberi,[1]* S. Leroy,[1] E. d'Acremont,[1] N. Bellahsen,[1] C. Ebinger,[2] A. Al-Lazki[3] and A. Pointu[1]

[1] *Laboratoire de Tectonique, University of Paris* 6 *UMR-CNRS* 7072, 4 *place Jussieu,* 75252 *Paris Cedex* 05, *France. E-mail: hritel.iberi@lgs.jussieu.fr*
[2] *Geology Department, Royal Holloway University of London, UK*
[3] *College of Sciences, Sultan Qaboos University, Sultanate of Oman*

Accepted 2006 November 9. Received 2006 November 6; in original form 2006 July 20

SUMMARY

Here we use receiver function analysis to retrieve crustal thickness and crustal composition along the 35-My-old passive margin of the eastern Gulf of Aden. Our aims are to use results from the 3-D seismic array to map crustal stretching across and along the Aden margin in southern Oman. The array recorded local and teleseismic events between 2003 March and 2004 March. Seventy-eight events were used in our joint inversions for Vp/Vs ratio and depth. The major results are: (1) Crustal thickness decreases from the uplifted rift flank of the margin towards the Sheba mid-ocean ridge. We found a crustal thickness of about 35 km beneath the northern rift flank. This value decreases sharply to 26 km beneath the post-rift subsidence zone on the Salalah coastal plain. This 10 km of crustal thinning occurs across a horizontal distance of less than 30 km showing a localization of the crustal thinning below the first known rifted block of the margin. (2) A second rift margin transect located about 50 km to the east shows no thinning from the coast to 50 km onshore. The lack of crustal thickness variation indicates that the maximum crustal stretching could be restricted to offshore regions. (3) The along-strike variations in crustal structure demonstrate the scale and longevity of the regular along-axis rift segmentation. (4) Extension is still observed north of the rifted domain, 70 km onshore from the coast, making the width of margin larger than first expected from geology. (5) The crust has a felsic to normal composition with a probably strong effect of the sedimentary layer on the Vp/Vs ratio (comprised between 1.67 and 1.91).

Key words: crustal structure, Receiver function, rifted margin, segmentation, seismology.

1 INTRODUCTION

The process of strain localization preceding the onset of seafloor spreading is still poorly understood, although extensively studied along passive continental margins worldwide. Current models of continental break-up processes differ in the geometry and distribution of strain, and the presence or absence of magmatism along conjugate margins (e.g. Frederiksen & Braun 2001; Buck 2004). One key constraint needed to differentiate between models for passive margin formation is a map of the crustal thickness variations from the uplifted rift flanks to the ocean–continent boundary. Its lateral variation is an important parameter in understanding the influence of pre-rift structure and tectonic processes involved in the deformation, and it provides clues into the formation and evolution of oceanic transform zones.

Seismic receiver functions are typical tools used to image the major discontinuities within the crust and the upper mantle (Langston 1977). Of particular interest is their ability to estimate the crust–mantle boundary (Moho). Maps of this interface give information on whether the deformation was localized or distributed, and where the thinning has occurred during the break-up process. They also provide estimates of the average Poisson's ratio for the crust, allowing one to evaluate lateral variations in crustal composition.

The eastern Gulf of Aden represents a natural laboratory to study passive continental margin evolution for many reasons: post-rift sedimentary strata are relatively thin, syn- and post-rift strata crop out onshore and are well-exposed, accurate conjugate margin reconstructions exist (e.g. Cochran 1981; d'Acremont *et al.* 2005, 2006). Although the syn- and post-rift sequences are well-mapped onshore, only exploratory well and shallow seismic data had been available to map subsurface structure beneath this youthful passive continental

---

*Geophysics Department, Stanford University, 397 Panama Mall, Mitchell Bldg., Stanford, CA 94305, USA.

margin. From 2003 March to 2004 March, a temporary network of 11 broad-band seismic stations operated along the southern coast of Oman, in the Dhofar area. This array permits us to extend geophysical investigations recently made offshore of the Gulf of Aden to onshore areas (Leroy *et al.* 2004; d'Acremont *et al.* 2005, 2006). We used this array to retrieve the crustal structure beneath each sensor. We address the following questions: What is the geometry of the crustal thinning along and across the strike of the basin and its uplifted flanks? How is it related to the pre-rift structure? Does the crustal composition vary along the strike of the margin? We first provide an overview of the regional tectonic setting, before presenting the receiver function method. We use here the technique recently proposed by Zhu & Kanamori (2000), that allows us to retrieve both crustal thickness and Vp/Vs ratio. Moreover, this method uses the converted phase Ps to the Moho together with its multiples ($PpPs$ and $PpSs$+$PsPs$). This combination of phases significantly reduces the trade-off that exists between the crustal thickness estimation and the velocity of the crust (Zandt & Ammon 1995). Next, we present the results of our investigations and discuss them in terms of extension and crustal composition for the non-volcanic northern margin of the eastern Gulf of Aden.

2 TECTONIC SETTINGS

The Gulf of Aden is a young oceanic basin that is one arm of the RRR Afar triple junction with the East African and Red Sea rifts. The Gulf of Aden separates Arabia from the Somalia plate. It extends from the Owen fracture zone to the east, and into the Afar depression to the west (Fig. 1). The mean extension direction N020 is oblique to the average trend of the Gulf of Aden N075, with an increasing extension rate from west (1.6 cm yr^{-1}) to east (2.3 cm yr^{-1}; Jestin *et al.* (1994); Fournier *et al.* (2001)). The oceanic spreading started at least at 17.6 Ma in the eastern part of the Gulf (Leroy *et al.* 2004), whereas seafloor spreading in the western part seems to continue to propagate westward into the Afar depression (Cochran 1981; Huchon & Khanbari 2003). The existence and development of the Gulf of Aden is often related to the presence of the Afar hotspot. Although volcanism in the Afar plateau region commenced at ~40 Ma (e.g. Ebinger *et al.* 1993; Kieffer *et al.* 2004), the highest eruption rates coincided with the initial rifitng of the southern Red Sea and Gulf of Aden at ~30 Ma (e.g. Courtillot *et al.* 1999; Ukstins *et al.* 2002; Wolfenden *et al.* 2005). The proximity to a mantle upwelling has resulted in the formation of a volcanic margin in the western Gulf of Aden (Tard *et al.* 1991), and a non-volcanic margin in its eastern part (Leroy *et al.* 2004; d'Acremont *et al.* 2005). The pre- and syn-rift stratigraphies along the western volcanic margins are masked by Oligo-Miocene lavas from the plume. The non-volcanic eastern margins, however, are the unique location of well-exposed break-up structures, and the conjugate margins are only 200 km apart. We focus our study on the northern non-volcanic margins in the Dhofar area, in Oman. Its conjugate margin is Socotra island (Yemen) and Somalia.

The margin comprises the same sequences as in the main Arabian platform: Cretaceous to Eocene marine platform sequences (Hadhramaut Group) overlying Precambrian to Cambrian basement (Fig. 2). The basement is composed of metamorphic rocks (gneiss and granodiorites) with intrusive Ordovician to Devonian dykes. The Hadramaut Group is composed of carbonate deposits and its thickness decreases towards the south due to the general uplift of the Arabian platfom. Roger *et al.* (1989) evaluate the thickness of this pre-rift sequence to be about 2 km in the Dhofar area (Fig. 2) that is confirmed by a well in Salalah plain. All of these sequences are cut by several fault-bounded syn-rift basins striking from N70°E to N110°E (Lepvrier *et al.* 2002; d'Acremont *et al.* 2005; Bellahsen *et al.* 2006). The major syn-rift basins exposed onshore are the Salalah basin and the Ashawq basin, bounded in the north by the Jabal Qara fault (Fig. 3). They are partly filled by Oligo-Miocene sediments of the Dhofar group (syn-rift, Fig. 2), and the Fars group (post-rift, middle to upper Miocene) (Roger *et al.* 1989; Platel &

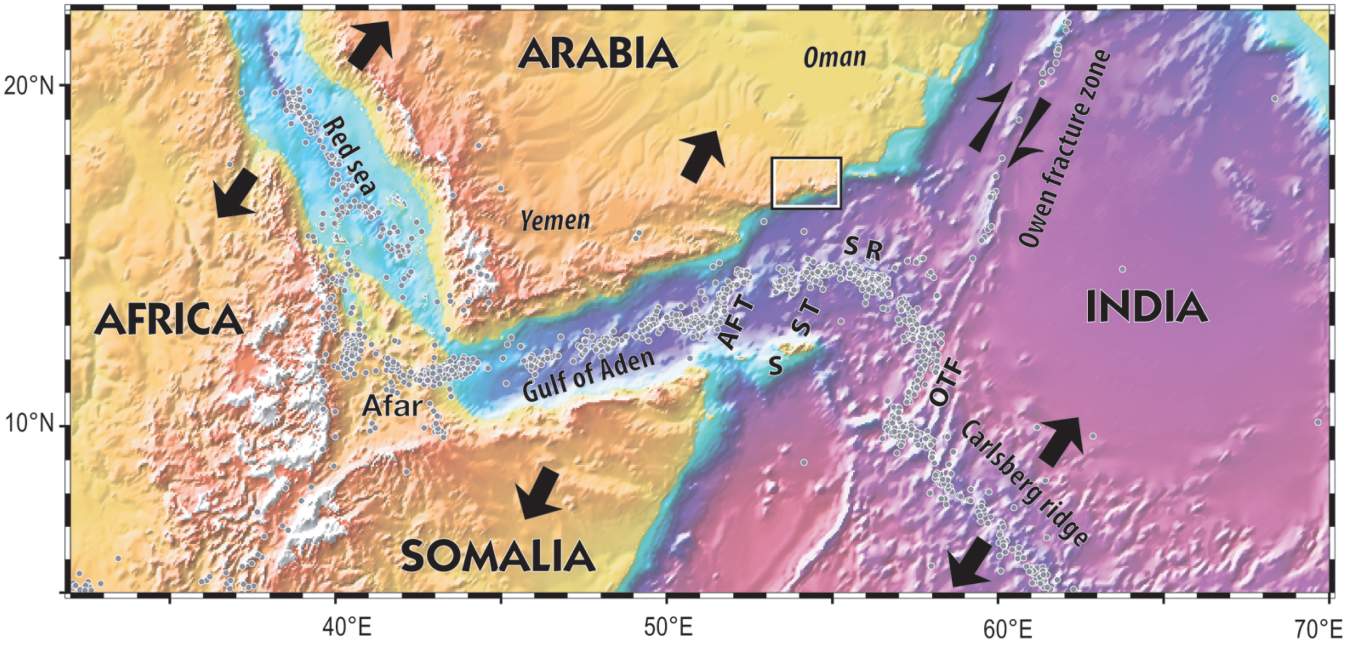

Figure 1. General tectonic background for the study area. The opening directions are indicated for the Africa, Somalia and Arabian plates. Also indicated are the Alula-Fartak transform fault (AFT), Socotra transform fault (ST), Socotra island (S), the Sheba Ridge (SR) and the Owen transform fault (OTF). Seismicity is displayed by grey circles, and the study area (Dhofar) is indicated by the black rectangle.

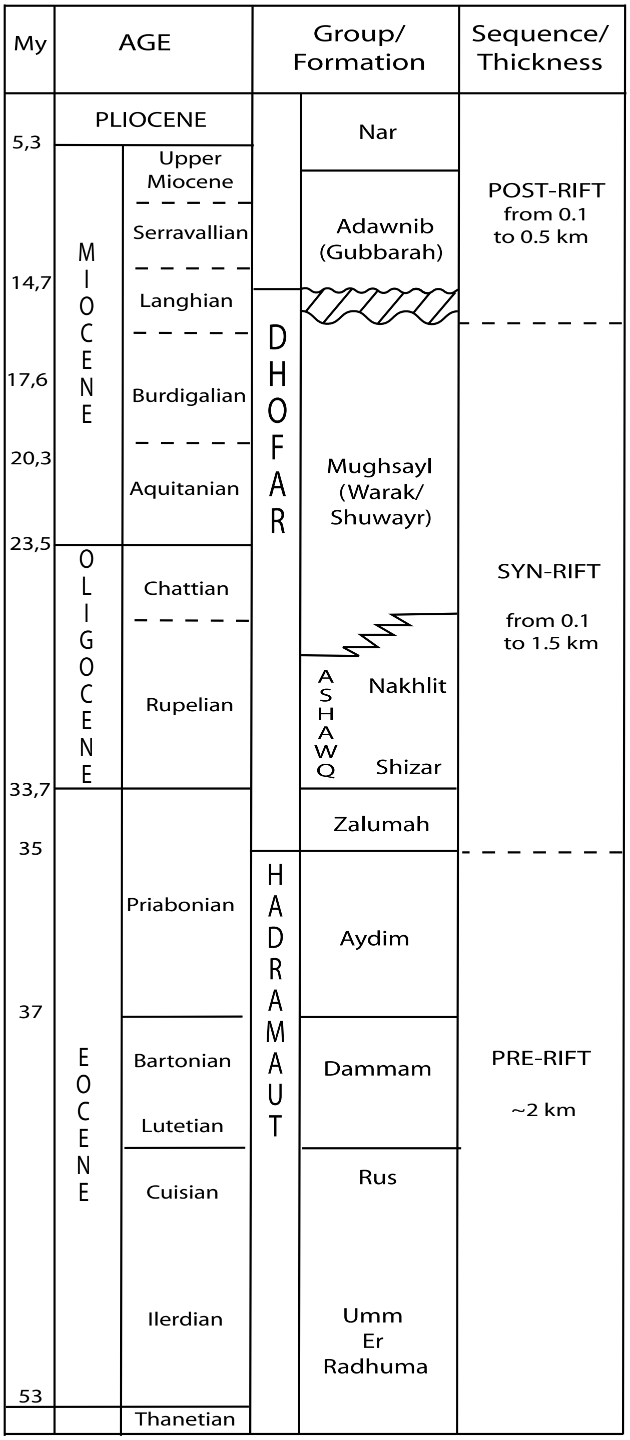

Figure 2. Stratigraphic column that shows the main sedimentary sequences retrieved within the Dhofar area. The expected thickness of each formation is given in the right-hand column of the table (modified from Roger *et al.* (1989)).

Roger 1989). In the north, the Haluf basin is the first known graben of the margin filled by early syn-rift sediments (Fig. 3). The Sala'Afan Basin, north of Mirbat is an N110°E trending Oligocene basin where the syn-rift sediments were partly eroded.

Recently, the Encens-Sheba/MD117 geophysical survey was performed between the Alula-Fartak and the Socotra fracture zone to constrain the structure and evolution of the conjugate margins as well as mode of extension prior to the break-up by reconstructing the margins (Leroy *et al.* 2004; d'Acremont *et al.* 2005, 2006). The non-volcanic margins and the ocean continent transition are segmented by two N027°E trending transfer fault zones and a complex non-uniform opening by an arc-like initiation of seafloor spreading in the OCT. The early oceanic segmentation shows a close correspondence to the late syn-rift stage segmentation (d'Acremont *et al.* 2005). An abnormally thin crust (between 1 and 4 km) inferred from the gravity study, abuts against the true oceanic crust where magnetic anomalies are easily identified. They suggest that mantle exhumation initially occurred prior to spreading at low extension rates in a magma-limited environment (d'Acremont *et al.* 2006). However, no link has been made so far with the onshore crust and upper-mantle structure.

3 CRUSTAL STRUCTURE BENEATH THE ARABIAN PLATE

Whereas crust and upper-mantle structure beneath central Arabia has been probed with geophysical methods (e.g. Mooney *et al.* 1985; Al-Amri 1998, 1999; Al-Lazki *et al.* 2002), the subsurface structure of southern Oman remains virtually unexplored. From deep seismic profiles, Mooney *et al.* (1985) propose a crustal and upper-mantle structure divided into 5 layers. The crustal velocities deduced from their work range from 6.0 to 6.9 km s^{-1}, with a crustal thickness of about 40–50 km across the Arabian Shield. Al-Amri (1998) estimates the crust in the Arabian platform to be more than 40 km with velocities varying between 5.5 and 7.6 km s^{-1} for a mean of 6.6 km s^{-1}. From a waveform modelling study, Rodgers *et al.* (1999) propose a mean crustal thickness of about 40 km with a mean velocity of 6.1 km s^{-1} and a Poisson's ratio of 0.27. In the northeastern part of Oman, Al-Lazki *et al.* (2002) take a mean crustal Vp between 6.4 and 6.6 km s^{-1}. More recently, a receiver function analysis in Saudi Arabia has been performed that proposes estimation of Vp/Vs ratio ($\sim$1.75) and crustal thickness for a Vp estimate of about 6.5 km s^{-1} (Al-Damegh *et al.* 2005).

However, little is known about the structure and velocity of the southern part of the Arabian platform. The receiver function analysis is strongly dependent on the initial P-wave velocity value, and our network doesn't overlay the same tectonic units (Fig. 3). Unfortunately, no refraction profiles in this region are available, and we can't rely on this kind of information to estimate the average crustal velocity we need in our method. From the global review of Christensen & Mooney (1995), the average crustal velocity for platforms is 6.4 and 6.2 km s^{-1} for an extended crust. The metamorphic rocks and granodiorites that compose basement in our studied area could present a P-wave velocity ranging between 6.1 and 6.7 km s^{-1} from Christensen & Mooney (1995). For stations on basement only, we thus used a mean crustal velocity of 6.3 km s^{-1}, based on the previous works formerly cited. The sedimentary layers in the study area are made of carbonate sediments of 4 km thickness. Their velocity can vary between 4.0 and 5.4 km s^{-1}, even less for the post-rift sequence (Mavko *et al.* 1998). We used an average velocity of 6.2 or 6.15 km s^{-1} to account for 1–2 km of limestones. The station in Salalah (S01, Fig. 3) is above the whole sequence (pre- syn- and post-rift) with alluvial deposits that can present P-wave velocity lower than 1.7 km s^{-1}. We then choose a mean P-wave velocity of 5.8 km s^{-1} in that case.

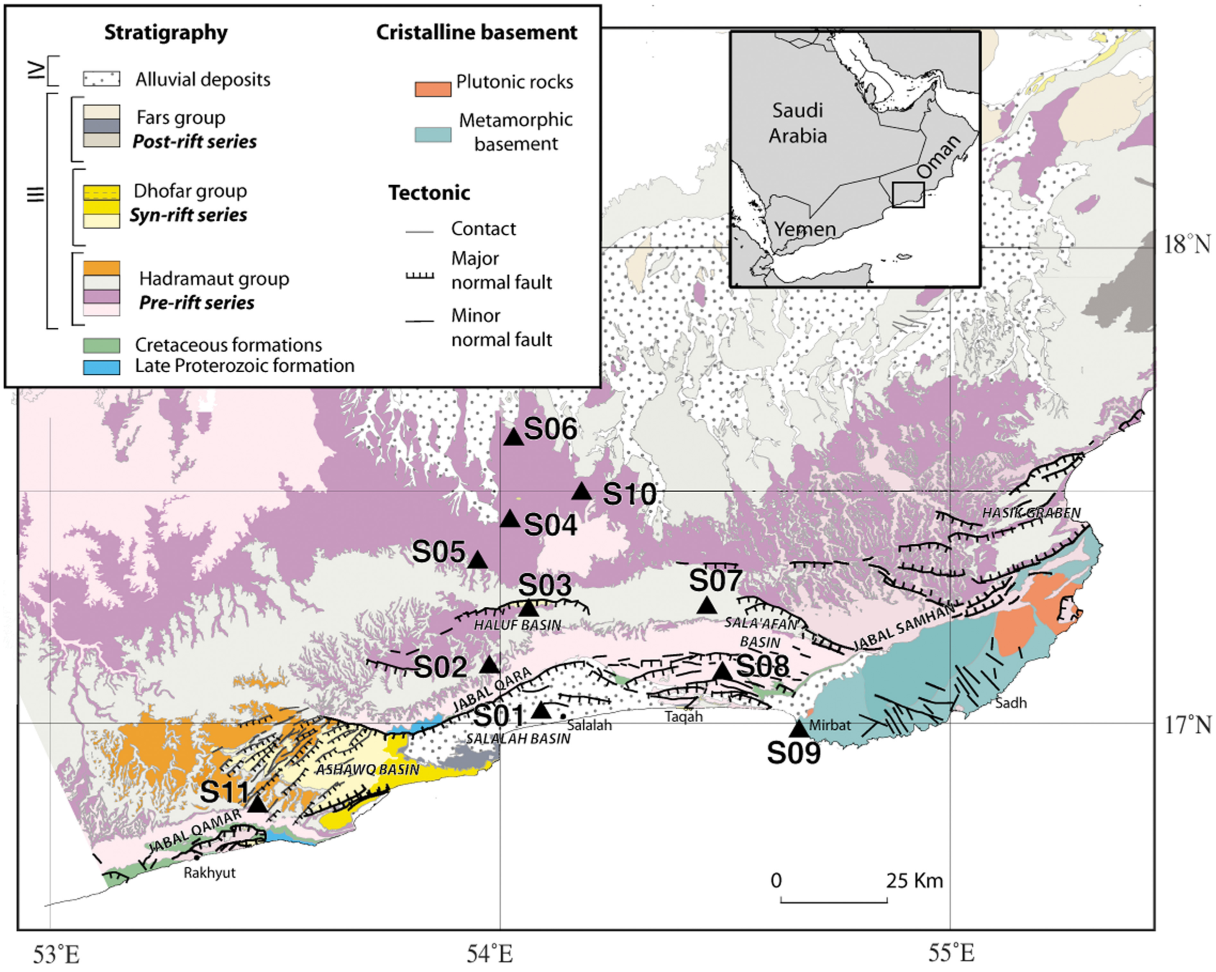

Figure 3. Geological map of the Dhofar region, southern coast of Oman (modified from Roger *et al.* 1989; Platel & Roger 1989) and location of the Dhofar temporary network. Eleven broad-band stations recorded sparse local, regional, and teleseismic events from 2003 March to 2004 March. The triangles represent the three-component stations used in this study, with their names adjacent to their locations. The main boundary faults for the Oligocene–Miocene basins are highlighted and we reported the names of the associated rift basins.

4 DATA

We installed a temporary network of 11 broad-band stations in the Dhofar area in 2003 March. These stations are Güralp 3-components CMG-40TD seismometers with a natural period of 30 s, recording with a sampling rate of 50 s.p.s. The instruments recorded continuously for one year. Servicing was performed on the field every 4 months to download the data and check the overall state of the instruments. We deployed the stations along main roads (Fig. 3), in fenced areas to ensure their safety from grazing animals.

We use seismograms from teleseismic events located between 30° and 95° epicentral distance and with magnitude over 5.5 (Fig. 4). We work on 78 particular events chosen to minimize the effects of dipping layers and anisotropy, as outlined in the methodological part below. Their azimuthal distribution is not evenly distributed, with a concentration of events in the E-NE direction due to the Philippines, Japan and Indonesia zones of subduction (Fig. 4). However, some good events were recorded from the mid-Atlantic ridge (West) and Indian ridge (South) filling the gaps. We have windowed the waveforms 5 s before and 40 s after the first *P*-wave arrival.

5 METHOD

5.1 The receiver functions

Receiver functions are now widely used to obtain depth estimates of crustal and/or mantle interfaces under three-component short- or broad-band seismic arrays (e.g. Vergne *et al.* 2002; Julià & Meijìa 2004). This method consists of isolating the *P*- to *S*-wave conversions (*Ps*) generated at major interfaces to retrieve the depth of this interface. The *Ps* traveltime is dependent on crustal thickness, mean crustal velocity (either Vp or Vs), and Vp/Vs ratio, so that a strong trade-off arises between the crustal thickness (H) and the velocity information (Ammon *et al.* 1990). Zandt *et al.* (1995) noticed that the use of traveltimes for the multiple phases *PpPs*, and *PpSs*+*PsPs* helps to constrain both crustal thickness and Vp/Vs ratio. Because the *Ps* waves are predominant on the radial component, the receiver functions are obtained by deconvolving the vertical component from the horizontal (Langston 1979; Ligorria & Ammon 1999). The deconvolution process can be made either in the frequency (Langston 1979) or in the time domain (Ligorria & Ammon 1999). After the deconvolution, radial and tangential components should be investigated with careful review. Indeed, a strong signal on the tangential

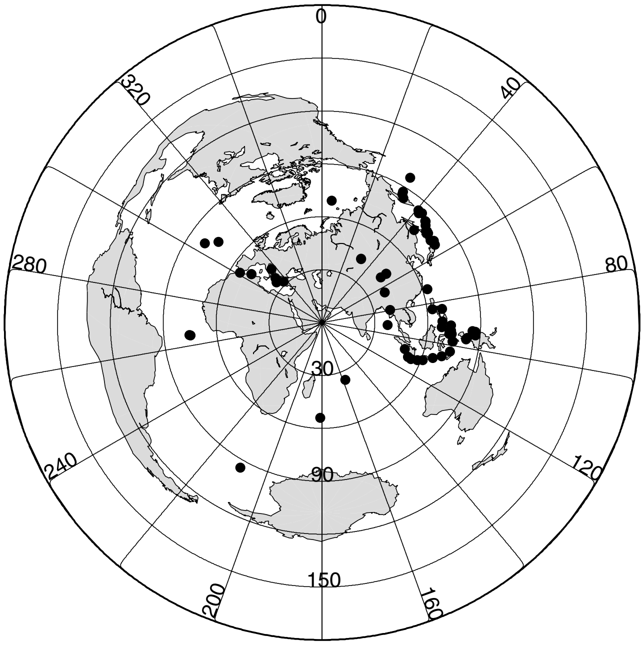

Figure 4. Azimuthal distribution for the 78 teleseismic events selected for the receiver function. The projection has been centred on the network, in the Dhofar area.

component could be indicative of dipping interfaces or anisotropy beneath the array, and the assumptions made for the receiver function analysis could then be incorrect (e.g. Jones & Phinney 1998, for a review). The amplitude of the *P*-to-*S* conversion phase is often very weak, and a stacking process is frequently used to enhance the signal-to-noise ratio. Recently, Zhu & Kanamori (2000) developed a stacking technique using *P*-to-*S* conversion phases and their multiples to obtain both crustal thickness and Vp/Vs ratio estimate. Their method consists of summing the amplitudes for theoretical arrivals for *Ps*, *PpPs*, and *PpSs*+*PsPs* (Fig. 5), and finding the H and κ values for which the stacking amplitudes are maximum. The use of the multiple converted phases is a particularly efficient way to reduce the ambiguity between H and κ (Zandt & Ammon 1995).

The stacking equation for N receiver functions should be summarized by the following:

$$S(H,\kappa) = \sum_{j=1}^{N} w_1 rf_j(t_1) + w_2 rf_j(t_2) - w_3 rf_j(t_3). \qquad (1)$$

S is called the objective function, and it is a maximum when all three phases are stacked coherently with the most likely (H, κ) couple. The indices 1–3 refer to the converted phases *Ps*, *PpPs*, and *PpSs*+*PsPs*, respectively. The amplitudes or the receiver function rf_j, ($j = 1$, N) are weighted by the terms w_1, w_2 and w_3, whose sum should be equal to one. The predicted arrival times (t_1, t_2 and t_3) are calculated using the following equations:

$$t_{Ps} = t_1 = H.\left[\sqrt{\left(1/V_s^2 - p^2\right)} - \sqrt{\left(1/V_p^2 - p^2\right)}\right] \qquad (2)$$

$$t_{PpPs} = t_2 = H.\left[\sqrt{\left(1/V_s^2 - p^2\right)} + \sqrt{\left(1/V_p^2 - p^2\right)}\right] \qquad (3)$$

$$t_{PpSs+PsPs} = t_3 = 2H.\sqrt{\left(1/V_s^2 - p^2\right)} \qquad (4)$$

with p the ray parameter. There are numerous advantages to the use of this method. Among others, it computes the arrival time with the real ray parameter of the event; an average crustal thickness is obtained by considering events from different directions; there is no need to pick arrivals that are sometimes indiscernible on the records. Another advantage of this method is the estimate of the error on both H and κ. Zhu & Kanamori (2000) first used the flatness of $S(H, \kappa)$ at the maximum to deduce standard errors. However, as recently mentioned by Julià & Meijìa (2004), this method does not consider the dependence of the two parameters, and a now widely used method to estimate uncertainties is a bootstrap algorithm (Efron & Tibshirani 1991). This method calculates statistics over a great number of subsets of data, randomly generated from the original data set (see e.g. Chevrot & van der Hilst 2000; Julià & Meijìa 2004).

5.2 The Dhofar Seismic experiment

The general method described above has been applied to our temporary network in Dhofar (Oman) to retrieve the crustal thickness and Vp/Vs ratio in this region. Over our whole data set, we first select 78 events with low signal on the transverse component (Fig. 6) to ensure minimal interference due to anisotropic and dipping media. We deconvolve the vertical component from the horizontal ones using the iterative time domain technique of Ligorria & Ammon (1999) with a Gaussian filter of 2.0 s. To ensure the highest quality of the receiver function, we only select events that reproduce more than 85 per cent of the original radial waveform (receiver function convolved with vertical waveform Ligorria & Ammon 1999). We then apply the stacking technique of Zhu & Kanamori (2000) on our data set to retrieve both H and κ. We have tested different values for the weights w_1, w_2 and w_3 in eq. (1). Little or no difference is noticed on the crustal thickness and κ values when changing the relative importance of these parameters. Our data show the maximum energy for the *P*-to-*S* conversion, and most of the stations show a signal from the *PpPs* as well as the *PpSs*+*PsPs* conversion. We then chose values of $w_1 = 0.6$, $w_2 = 0.3$ and $w_3 = 0.1$ for most of our stations in this study. When possible, however, we increase the weight of *PpSs*+*PsPs* conversion to enhance the maximum of the objective function during the stacking. In this case, we prefer the following values $w_1 = 0.5$, $w_2 = 0.3$ and $w_3 = 0.2$. To estimate

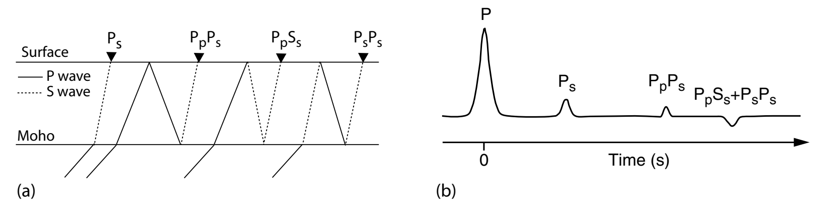

Figure 5. (a) The Moho converted phases *Ps*, and its multiples *PpPs*, and *PpSs*+*PsPs*. (b) Theoretical receiver function for the converted phases shown on (a). The arrival time of the different picks depends on the depth of the interface, the incidence angle, and the *P* and *S* wave velocities.

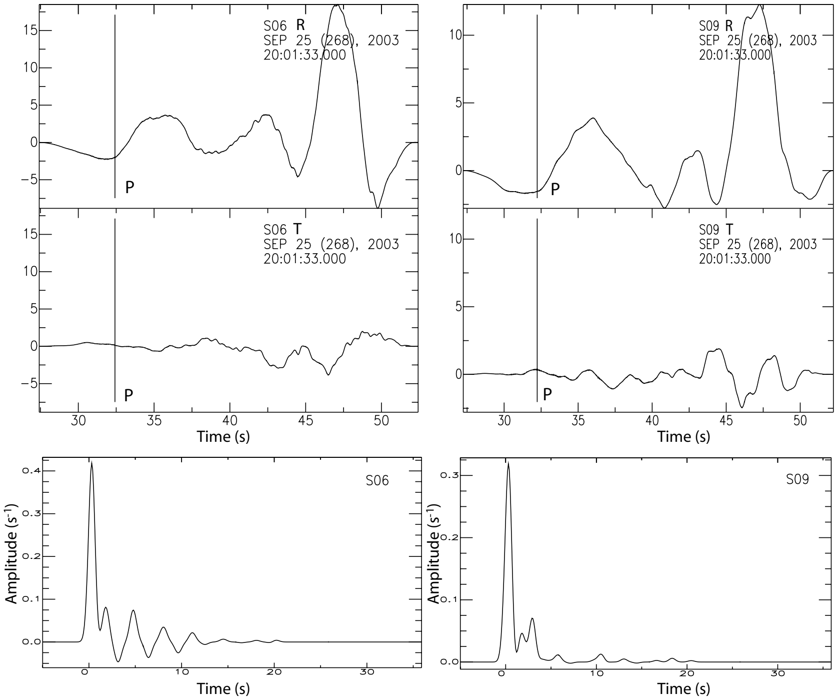

Figure 6. Example for radial and transverse components with receiver function for two stations S06 (left) and S09 (right). Upper panel is the radial component and middle panel represents the transverse component with the same amplitude scale. We can see that the signal on the transverse (T) is weaker than the radial one (R). Bottom panels represent the receiver function for both stations S06 and S09 after iterative deconvolution in the time domain.

Table 1. Summaries of the receiver function results for all the stations. We refer to the stations using their numbers. *Vp* refers to the mean crustal velocity taken for the calculation of the crustal thickness (*H*) and the *Vp*/*Vs* (κ) ratio.

Station	Latitude	Longitude	Altitude (km)	nb. events	Vp (km s^{-1})	$w_1\ w_2\ w_3$	H (km)	Vp/Vs (κ)
S01	17.027	54.113	0.00	38	5.80	0.6 0.3 0.1	28.6 ± 0.6	1.86 ± 0.04
S02	17.126	53.996	0.79	50	6.20	0.6 0.3 0.1	26.6 ± 2.6	1.87 ± 0.06
S03	17.250	54.084	0.89	45	6.15	0.6 0.3 0.1	32.2 ± 0.4	1.76 ± 0.02
S04	17.444	54.042	0.61	26	6.20	0.5 0.3 0.2	36.6 ± 0.4	1.77 ± 0.01
S05	17.354	53.968	0.68	32	6.20	0.6 0.3 0.1	34.0 ± 2.1	1.89 ± 0.06
S06	17.621	54.051	0.48	41	6.20	0.5 0.3 0.2	32.4 ± 0.6	1.89 ± 0.02
S07	17.255	54.488	0.94	32	6.20	0.6 0.3 0.1	28.2 ± 2.7	1.91 ± 0.06
S08	17.113	54.523	0.66	6	6.20	0.6 0.3 0.1	27.6 ± 3.7	1.81 ± 0.10
S09	16.986	54.697	0.00	32	6.30	0.5 0.3 0.2	29.2 ± 0.8	1.67 ± 0.02
S10	17.503	54.204	0.55	51	6.20	0.5 0.3 0.2	32.4 ± 0.8	1.75 ± 0.03
S11	16.823	53.470	1.01	45	6.20	0.5 0.3 0.2	25.6 ± 2.6	1.77 ± 0.07

the uncertainty on our H and κ results, we employ the bootstrap approach, as adviced by numerous authors (e.g. Chevrot & van der Hilst 2000; Julià & Meijìa 2004). We randomly generate 200 data subsets from the original receiver functions data set. We then calculate H and κ for each subset with the Zhu & Kanamori (2000) stacking method. Finally we estimate standard error with classic statistic formulae from the covariance matrix.

6 RESULTS

In this section, we detail the results obtained from the receiver function analysis for each station (Fig. 3, Table 1). We checked the performance of the stacking method by plotting the traveltimes corresponding to the maximum of the objective function against the receiver functions (e.g. Fig. 7). This provides an easy check of the results by visually comparing the observations and the estimated conversion times.

6.1 Salalah (S01)

Station S01 was located in the main city Salalah, and it is characterized by a low signal-to-noise ratio. This is coming first from its closeness to main and noisy roads, and second from its location in the Salalah basin filled with post-rift sedimentary strata (Fig. 3). However, 38 events of good quality have been stacked in the (H, κ) domain (Fig. 7). The P-to-S conversion occurs around 5 s after the direct P pick. When restraining the search in the H, κ domain to within (20–50 km) and (1.6–2.0), respectively, we obtain a maximum in the objective function for $H = 28.6 \pm 0.6$ km and $\kappa = 1.86 \pm 0.04$. We observed a clear conversion 1 or 2 s after the direct P (Fig. 7), hereafter referred to as Px. We expect this signal to be caused by a mid-crustal discontinuity beneath S01. The Salalah basin is filled with up to 1.5–2 km of syn- and post-rift carbonates and clastics. The total depth to metamorphic basement could be as much as 3 km (Fig. 2, Roger *et al.* 1989). However, it is highly probable that this Px phase is a multiple of a

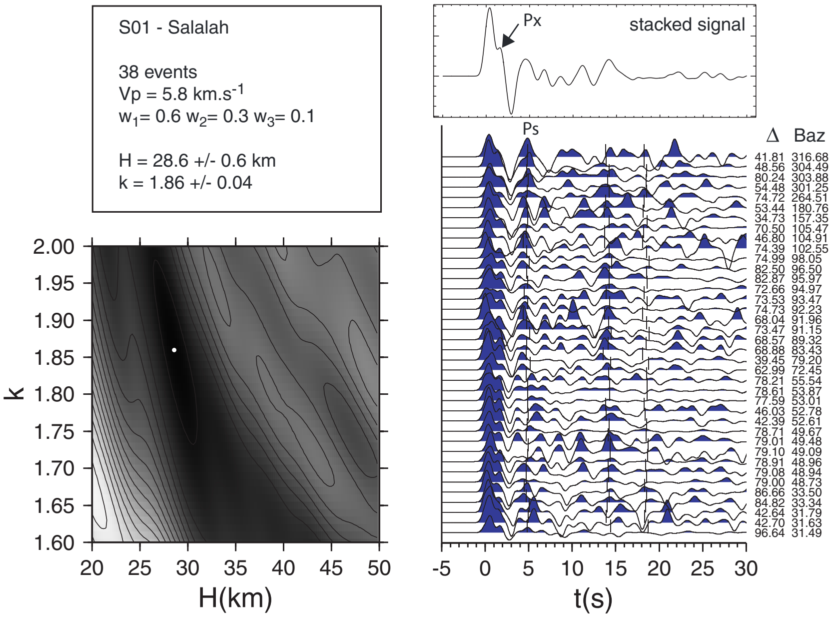

Figure 7. Crustal thickness estimate for the station S01, Salalah. The left panel is the grid search method in the (H, κ) domain (following Zhu & Kanamori 2000, technique). The grey scale is indicative for the amplitude of the objective function $S(H,\kappa)$ (eq. 1). High amplitude is indicated by dark colour. The maximum is marked by the white point and corresponds to the value in the onset. The right panel represents the receiver function for the 38 events used for S01, organized by increasing backazimuth (baz). The epicentral distance is also indicated (Δ) and the stacked signal is represented above. The Px marker indicates intracrustal conversion phase.

mid-crustal discontinuity, and not the direct conversion. First its shape is immediately followed by a negative pulse that looks like a multiple. Second the direct *P* pick slightly but obviously shifted from the 0 toward the right is indicative of more than one pulse. To be able to distinguish all the pulses and to determine the depth of the mid-crustal reflector, we should reprocess the data with a separate treatment. Moreover, we should also investigate the possible constructive multiples resulting from the layering of the sediments. It is beyond the scope of this article to deal with these intracrustal structures, and work in progress should be published in a separate paper.

Given the high level of noise partially due to reverberation within the crustal layers, we tried to separate events according to different azimuths. These tests give estimates within the error bounds.

6.2 Ghado (S02)

This station is located North of Salalah, on the footwall of the Jabal-Qara border fault bounding the Salalah basin, above pre-rift sediment formation (Fig. 3). We stacked 50 events for this station (Fig. 8). The maximum of the objective function happens for $H = 26.6 \pm 2.6$ and $\kappa = 1.87 \pm 0.06$. This maximum is well defined in the (H, κ) domain (Fig. 8). We observed a coherent arrival *Px* 1.5 s after the direct *P* which shape changes with backazimuthal distances (Fig. 8). Once again, further analyses are needed in order to elucidate this intracrustal arrival. We suspect it to be the limit between basement and pre-rift sediments.

6.3 Queiroon (S03)

S03 is located between the Salalah basin and the Haluf graben in the north of the Jabal Qara fault. It overlies sediments of the Hadhramaut formation, justifying a slightly lower average *P*-wave velocity of 6.15 km s^{-1} (pre-rift, Fig. 3). We have used 45 events for the stacking technique for Queiroon (Fig. 8). For this station we found that weights of $w_1 = 0.6, w_2 = 0.3$ and $w_3 = 0.1$ give the best focus of the maximum in the objective function. The final result in the (H, κ) domain gives $H = 32.2 \pm 0.4$ and $\kappa = 1.76 \pm 0.02$. Some intermediate arrival appears about 1 s after the direct *P* whose shape varies slightly with backazimuth (Fig. 8). It could be either the basement–sediment boundary, or the Jabal Qara fault plane. This alternative will be investigated in a strictly crustal study later on.

6.4 Rawya (S04)

We have only stacked 26 events for this station located on pre-rift sediments (Fig. 3). Rawya did not record for three months, but the quality and quantity of data are adequate (Fig. 8). We obtain a likely value of 36.6 ± 0.4 km for the crustal thickness and 1.77 ± 0.01 for κ. Opposite to the previous stations, we used here weights of 0.5, 0.3 and 0.2 for w_1, w_2 and w_3, respectively. Once again, a very strong intermediate *Px* phase can be observed very close to the direct *P*-wave pick, about 1.5 s after.

6.5 Haluf (S05)

This station was located above the pre-rift sediment on the uplifted flank north of the Haluf graben, and had some power supply deficiency. However, we were able to stack 32 events with a good receiver function signal. The stacking technique in the (H, κ) domain shows a maximum at $H = 34.0$ km $\pm$ 2.1 and $\kappa = 1.89 \pm 0.06$. The estimated error is large, and is probably due to the fact that the multiple *PpPs* is not clearly observed on all the records. It is then difficult to independently determine H and κ, as shown by the elongated maximum in Fig. 8. Varying the weight values has little effect on the results ($H = 34.2$ and $\kappa = 1.89$ for $w_1 = 0.5, w_2 = 0.3$

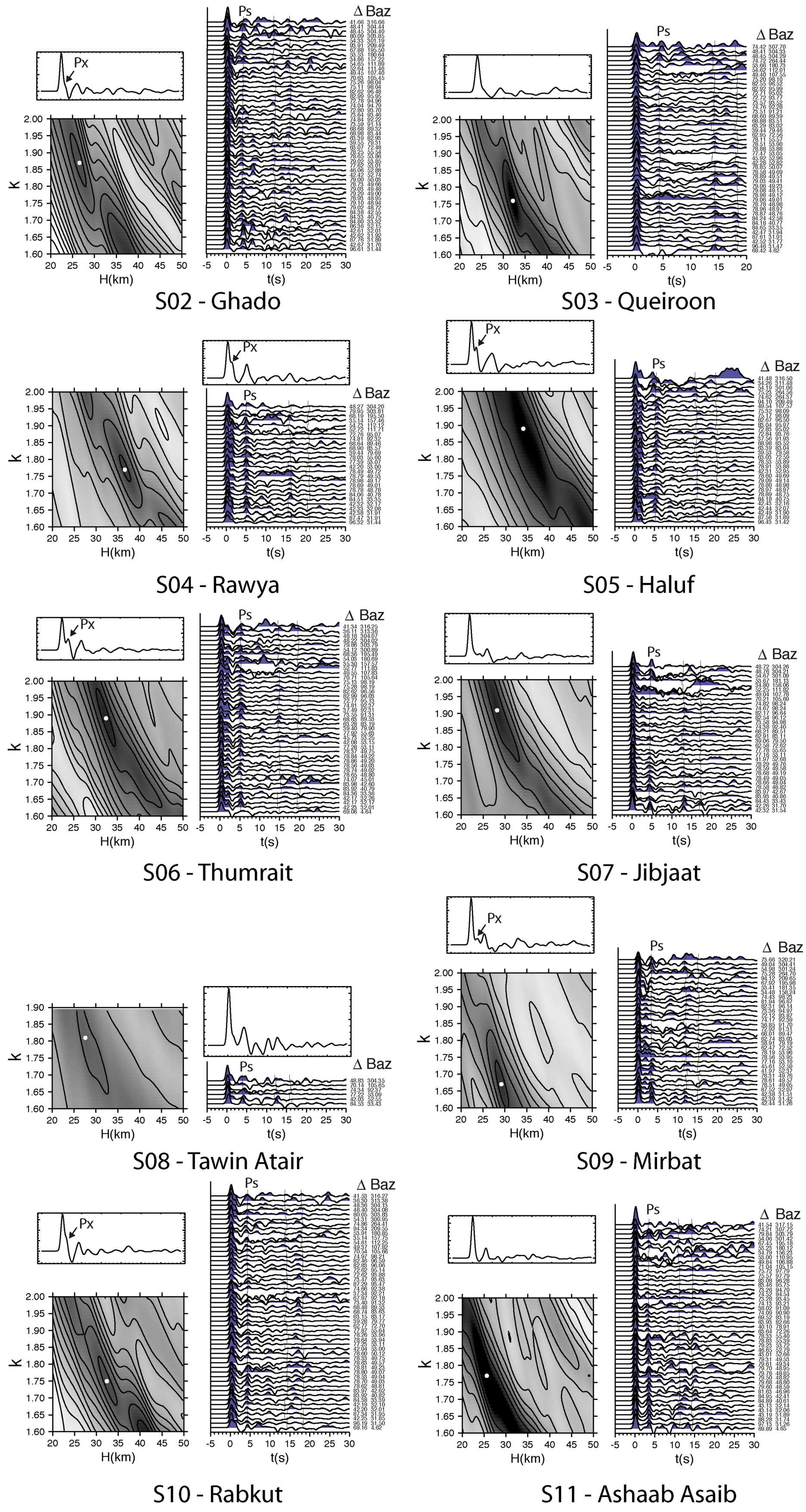

Figure 8. Crustal thickness estimate for the remaining stations of the network (S02–S11). For each station, the representation is the same as for Fig. 7.

and $w_3 = 0.2$). There is once more a strong *Px* arrival clearly observed 1.5 s after the direct *P* (Fig. 8).

6.6 Thumrait (S06)

Although the northeasternmost station of our network only recorded for 9 months, we were able to stack 41 events. When taking weighting factors of 0.5, 0.3 and 0.2 for w_1, w_2 and w_3, respectively, we obtain a more pronounced maximum at $H = 32.4$ km ± 0.6 and $\kappa = 1.89 \pm 0.02$ (Fig. 8). As for previous stations, we observed an intermediate arrival 2 s after the direct *P*.

6.7 Jibjaat (S07)

S07 was installed in the western part of the Oligo-Miocene Sala'afan graben, on the eroded pre-rift sedimentary formation (Fig. 3). We took $w_1 = 0.6, w_2 = 0.3$ and $w_3 = 0.1$ to stack the 32 selected events of this station. The stacking in the (H, κ) domain gives us a crustal thickness of 28.2 km ± 2.7 and $\kappa = 1.91 \pm 0.06$. There is no clear systematic intermediate arrival on the records (Fig. 8), and a classic stack of the receiver functions doesn't enhance any intermediate conversion, either.

6.8 Tawin Atair (S08)

Tawin Atair is located on the eastern uplift flank of the Salalah basin, on pre-rift carbonates (Fig. 3). This station recorded for only a short period of time, and few events were available for the receiver function analysis. We used six events that confidently reproduce 85 per cent or more of the original radial component during the iterative deconvolution. Stacking these six receiver functions in the (H, κ) domain (Fig. 8), we obtain a maximum of the objective function for a Moho depth of 27.6 km ± 3.7 and a κ value of 1.81 ± 0.1. The high uncertainty on these values stems from the few numbers of available records and the high noise level. We had little success even by trying to change the weighting parameters to focus the maximum of the objective function, and we had to restrict the area of κ value to less than 1.90 to avoid unrealistic cases. Moreover, because of low signal-to-noise ratio, we lack events to say with confidence whether or not an intermediate *Px* conversion is present in the signal (Fig. 8).

6.9 Mirbat (S09)

This station was located east of the network, in Mirbat city near the coast. It lies directly on crystalline Proterozoic basement in Mirbat town and thus shows a very low noise level (Fig. 3). For this station, we took an average *P*-wave velocity of 6.3 to account for the lack of sediment. We have stacked 32 receiver functions for Mirbat, and a well-located maximum for the objective function is found for a crustal thickness $H = 29.2$ km ± 0.8 and a κ value of 1.67 ± 0.02. Clear multiple conversion is observed (Fig. 8), allowing us to precisely determine both H and κ. We used $w_1 = 0.5, w_2 = 0.3$ and $w_3 = 0.2$ to account for this. We also noticed an intermediate conversion *Px* that arrives 1.5–2 s after the direct *P*, with a very clear backazimuthal dependancy. This can't be related to any sedimentary layers, but more probably to a fault plane.

6.10 Rabkut (S10)

This station was installed at the same location as a short period station of the permanent Oman network, on the pre-rift sediment constituting the Arabian platform (lower Eocene) in the north of the Haluf graben (Fig. 3). The site was very far from any disturbance, and the signal of S10 is very clear. Moreover, the station recorded continuously for the whole experiment. That allows us to stack 51 high quality receiver functions (Fig. 8). When letting the Vp/Vs ratio freely varying, we obtain unrealistic values of 41.0 km for the crustal thickness and 1.59 for the κ value. We then limit the range of κ values to be within 1.70 and 2.0. The Moho is then found to be at 32.4 km ± 0.8 depth, and the κ value is 1.75 ± 0.03 for weighting parameters of $w_1 = 0.5, w_2 = 0.3$ and $w_3 = 0.2$. There is less energy on the receiver function for this solution (Fig. 8), but we suspect that the signal observed around 16–17 s is coming from constructive multiples due to an intracrustal layer. This layer is evidenced by the presence of an intermediate conversion *Px* about 1 or 1.5 s after the first *P* pick.

6.11 Shahaab Asaib (S11)

This station is at the far west end of our network (Fig. 3), on the southern edge of the syn-rift Ashawq graben and the northern uplift flank of Rakyut syn-rift basin bounded by the Jabal Qamar. It is installed on the pre-rift sediments of Hadhramaut group (Fig. 3). We were able to stack 45 receiver functions for this station, with a good signal-to-noise ratio. The maximum of the objective function is found for a crustal thickness $H = 25.6$ km ±2.6 and $\kappa = 1.77 \pm 0.07$. The weighting factors we chose were $w_1 = 0.5, w_2 = 0.3$ and $w_3 = 0.2$ (Fig. 8). We observe no intracrustal conversion beneath S11.

7 DISCUSSION AND IMPLICATIONS

7.1 Error estimation

As previously mentioned, we estimate the uncertainty for both H and Vp/Vs ratio by a bootstrap analysis (Efron & Tibshirani 1991). However, this kind of method doesn't take into account the variability of the results relative to the choice of the initial *P*-wave velocity. In order to test the sensitivity of our results to this parameter, we reprocessed the stacking method for each station for 100 *P*-wave velocity values randomly chosen within a probable range of ±0.5 km s^{-1} around the initial value. Fig. 9 represents the ellipses of confidence deduced from the covariance matrix for both cases. The plain line represents the error coming from the stacking method itself whereas the dashed one represents the error coming from the choice of the initial *Vp* model. The latter has more influence on the estimation of crustal thickness, whereas the elongated shape at about 45° is well retrieved for the stacking method error. As a result, the observed variations of both H and Vp/Vs ratio are significant compared with the error estimated by the bootstrap methods, and thus reflect real characteristics of the crust we discuss hereafter. Our best estimates for the crustal thickness and the Vp/Vs ratio from the receiver function analysis are summarized in Fig. 10 and Table 1. The error estimation in Table 1 is coming from the classical bootstrap algorithm without changing initial average *Vp* value. To better discuss the results and their interpretation, we projected the results onto a profile that roughly runs north–south (from S01 to S06) nearly orthogonal to main rifting structures (faults striking from N110°E to N70°E). This profile allows us to compare surface structure to variations in Moho depth and the Vp/Vs ratio (Fig. 11). The crustal thickness ranges from *ca.* 25 km for stations near the coast to more than 36 km for the uplifted and largely unfaulted northern rift flank.

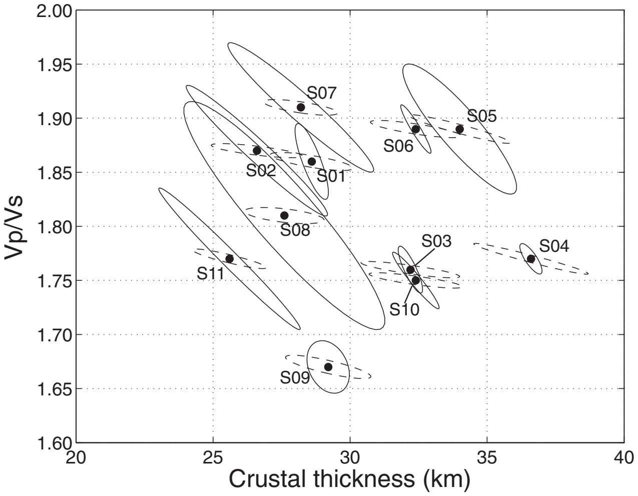

Figure 9. Deduced Vp/Vs ratio as a function of crustal thickness for the stations in Dhofar area. The error ellipses are indicated in plain line for the stacking method and in dashed lines for the uncertainty coming from initial Vp model variations. The variations both in Vp/Vs ratio and crustal thickness are greater than the error estimates and thus indicatives.

The Vp/Vs ratio ranges from 1.67 (for S09) to 1.91 (for S07), with a mean value of 1.81 (equivalent to a Poisson's ratio of 0.28). The average uncertainty we have on H is ± 1.5 km, and ± 0.04 for κ. The high uncertainties observed at some stations mainly stems from the fact that the amplitudes of the converted multiples is quite small (e.g., S11). Where the *PpPs* signal is clear, the uncertainty drops dramatically to less than ± 0.5 km for the Moho depth estimation, and ± 0.01 for κ (e.g. S04). It is clear from our grid search that the strong trade-off between H and κ is still present, even using the *PpPs* multiple (e.g. S05). The difficulty we have to use the *PpPs* and *PpSs*+*PsPs* conversion most likely comes from the multiple reverberations within intracrustal layers. These reverberations add more signal within the receiver function and the main conversions could then be blurred. The presence of a conversion phase 1–2 s after the direct P is a strong evidence for this kind of behaviour (e.g. Fig. 7).

7.2 The mid-crustal discontinuity

In addition to the main crust–mantle boundary, we find evidence for a mid-crustal interface under at least seven stations of the network. In these cases, clear conversion waves are observed 1–2 s after the first P-wave pick. However, we notice that these mid-crustal conversion waves are immediately followed by a negative pulse, and that the direct P-wave pick is most of the time-shifted from the 0 axis. These indicate a multiple phase and not a first P to S conversion. Moreover, for some station, the shape of this conversion changes with the backazimuth indicative of a dipping interface. Since the aim of this study is to use crustal thickness variations as strain marker for the continental break-up process, the study of these intracrustal events is beyond the scope of this paper and are the topic of a separate, more detailed study. Moreover, the presence of sediments has been taken into account in the average velocity values we take for the different stations.

7.3 The crustal thickness

The crust/mantle boundary is quite clear beneath all the stations of our array. Its variations are large enough to be significant relative to the error bars (Fig. 9). First, we discuss the previous estimates for crustal thickness of the Arabian platform with the results of our northernmost stations (S04, S06 and S10). Our estimates for this area are smaller than earlier estimates for the Arabian platform region. Al-Amri (1998) and Al-Amri (1999) found a Moho discontinuity at about 45 km depth, coherent with the study of Sandvol *et al.* (1998) at the station RIYD in Saudi Arabia. A lesser value of 40 km is proposed by Rodgers *et al.* (1999) for the Arabian platform with a totally independent method. However, the greater value we obtain is 36.6 km for station S04 (Rawya), and the northernmost station (S06-Thumrait) records a crustal thickness of about 32 km. Our estimate of mean crustal Vp is smaller than the one used by Al-Amri (1998) and thus could account for a thinner estimation of the crustal thickness. However, our tests with a Vp value of 6.5 km s^{-1} give a maximum result of 38 km for S04 (Rawya) and 34.5 km for S06 (Thumrait), still lower than the 45 km proposed by Al-Amri (1998). The thinner crust seen in this study thus indicates erosion and extension relative to stable interior of the Arabian platform, or it may indicate pre-rift lateral variations in crustal thickness. In the former case, the width of the margin is then larger than expected from geology.

We observe a general thinning of the crust toward the south, in the direction of the Sheba spreading ridge. The crust is more than 32 km thick for the northern stations (stations S04, S05, S06 and S10, Fig. 10), and decreases to 26 km thick near the coastline (stations

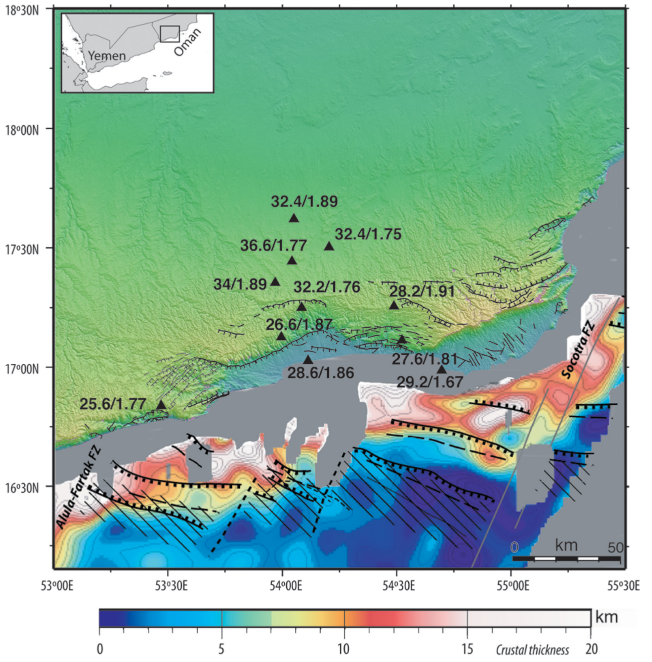

Figure 10. Crustal thickness results from our receiver function analysis for the 11 stations shown in Fig. 3. The stations are represented by the black triangles. The crustal thickness and the Vp/Vs ratio are reported adjacent to the station they are related to. The shallowest Moho is observed for the stations nearest to the coast, whereas we report the thickest crust northward. Onland normal faults are reported from Fig. 3 and offshore normal faults come from d'Acremont *et al.* (2005) studies. The colour scale represents the crustal thickness inferred from the offshore gravity data of the Encens-Sheba cruise (Leroy *et al.* 2004; d'Acremont *et al.* 2006). The grey and dashed lines represent the segmentation of the margin, the fracture and transfer zones, respectively. The hatched areas correspond to the ocean continent transition zones shifted by these accommodation zones of deformation. The topographic data come from SRTM (http://srtm.usgs.gov/).

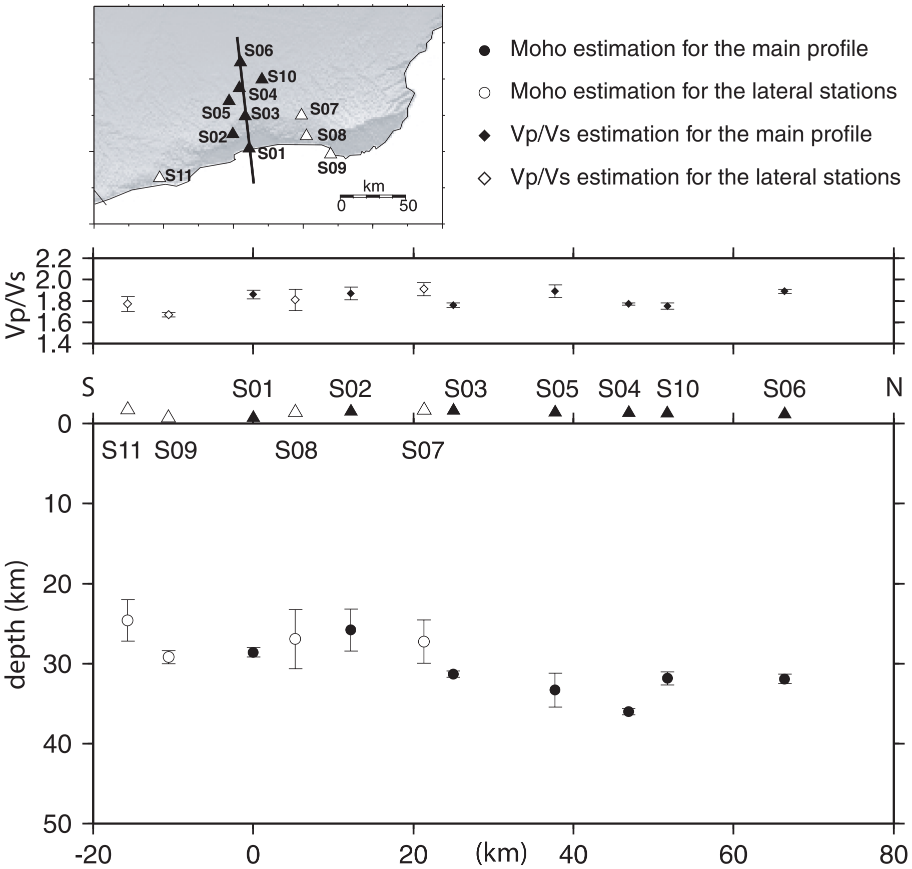

Figure 11. Cross-section along a roughly N-S profile, that runs from S01 to S06 roughly perpendicular to the strike of syn-rift basins (upper inset). The results for the Moho estimation are reported with circles. The stations along the main profile (S01, S02, S03, S04, S05, S06 and S10) are in black. The stations off the line of the profile are represented in white (S07, S08, S09 and S11). The upper panel represents the Vp/Vs ratio results for the stations on the same profile.

S01 and S11). This deflection is not uniform, and a sharp change is located between S02 and S03. At this position, there is a vertical Moho fluctuation of 6 km in less than 15 horizontal kilometres. The total thinning of the crust (about 10 km) happens in about 30 km, the Moho remaining quite flat south of S02 and north of S05 (Fig. 11). It is of importance to notice that we locate the major thinning of the crust between the Haluf graben and the Jabal Qara fault (Figs 3 and 10). It seems that the deformation has occurred beneath the first known fault block of the margin. This block shows syn-rift deposits on its exposed footwall. The Moho variations can then be explained either by isostatic thinning related to the formation of the basin at the surface, or stretching of the upper and lower crust. It is very likely that our network only samples a small window of the thinned crust, and that even a thinner crust is present offshore. The offshore gravity data modelling gives a crustal thinning southward from 17 km near the coast to 4 km in the ocean continent transition (Fig. 10, Leroy *et al.* 2004; d'Acremont *et al.* 2005, 2006). It is then difficult to relate those small patterns to general features of passive margins. Yet, it is very interesting to show that the decrease of the crustal thickness onshore is localized between the first fault of the margin and the main onshore fault. If we assume an initial crustal thickness ranging from 36 to 40 km for the Arabian platform (this study and Rodgers *et al.* 1999) and a final crust of about 26 km (station S11-Ashaab Asaib), the stretching factor β is then comprised between 1.38 and 1.54. Considering that the crust is thinning more dramatically southward, these estimates are lower bounds. The new OBS data collected in the area should enhance this question (Leroy *et al.* 2006).

We report lateral variations along the coast, with a deeper Moho East of Dhofar (ca. 28 km for S07, S08 and S09), and shallower values for S01, S02 and S11 (ca. 26 km). First, a simple calculation between S01 (Salalah) and S09 (Mirbat) shows that there could easily be an isostatic compensation between those two locations, considering the amount of sediments beneath S01. However, S11 (Shahaab Asaib) shows too thin crust and too high elevation to be isostatically compensated. This station is located on the uplifted flank of a syn-rift basin with outcropping Cretaceous sediments and bounded by the Jabal Qamar fault, very similar to the Salalah basin and the Jabal Qara fault (Fig. 3). S02 station (Ghado) could then be analogous to S11 situation. Second, the sharp change observed between S02 and S03 is not happening between S08 and S07 even if these stations are on the same latitude (Figs 10 and 11). S07 and S08 stations are both in the rifted basins in which syn-rift sediments have been eroded (Fig. 3). East of these stations, the Jabal Samhan scarp is one of the highest (ca. 1700 m). Yet, the syn-rift fault is located at sea, and we can expect the maximum crustal thinning in the south, offshore. d'Acremont *et al.* (2006) evidence a thinning of the crust correlated to the fracture zones and transfer faults. These behaviours enhanced the role of the segmentation of the margin to be one possible cause of lateral difference in our results. A variable lithospheric rheology and/or sediment thickness variations could explain these observations. We await the results of ongoing studies from a broader array to differentiate between these ideas.

7.4 The Vp/Vs ratio

The general deepening of the Moho towards the North we observed in our results could strongly affect our Vp/Vs ratio estimations (Fig. 10). Indeed, when the interface is dipping, the multiple traveltimes through the crust are different according to their direction. When travelling downdip, the multiples have shorter traveltimes than for a horizontal discontinuity. Conversely, multiples travelling updip show a longer traveltime than those generated at a horizontal interface. Subsequently, we will underestimate the value of Vp/Vs for waves travelling updip, and overestimate it for waves proceeding downdip (e.g. Jones & Phinney 1998; Julià & Meijìa 2004; Endrun *et al.* 2005). As most of our events are coming from the ENE quadrant (Fig. 4) and the dipping is maximum in a roughly NS direction, we expect our estimate of Vp/Vs ratio not to be significantly misvalued. Actually, the *Ps* conversion arrival shows no variation with the backazimuth of the events (see e.g. station S03 Fig. 8), indicative of low effect from a dipping Moho. Whenever it is, we predict a slightly overestimation of κ. In seismogenic zones, the Vp/Vs ratio is often related to fluid saturation in rocks (e.g. Latorre *et al.* 2004; Vanorio *et al.* 2005), but it could also be representative of the composition of the media and/or the presence of melt (e.g. Chrisensen 1996; Zandt & Ammon 1995). Even though no simple relation between Poisson's ratio and felsic and mafic rock composition exists, the increasing content of silica in the rocks decreases the Poisson's ratio (Chrisensen 1996).

The κ values we find range from 1.67 to 1.91 (Poisson's ratio from 0.22 to 0.31), with a mean value of 0.28 for the Poisson's ratio. This range is similar to the values found by Al-Damegh *et al.* (2005) for the Vp/Vs ratio (1.71–1.81). Our mean Poisson's ratio is greater than the mean one usually observed for the continental crust (0.265), and less than the mean value for the oceanic crust (0.30) (Zandt & Ammon 1995; Chrisensen 1996). However, it is of the same order of the estimate of Rodgers *et al.* (1999) for the Poisson's ratio of Arabian platform (0.27). In our case, it probably reflects the modified nature of the Dhofar crust in this region due to the break-up process, together with the influence of sedimentary cover. The presence of the sediment probably increase our estimation of the Vp/Vs ratio due to the presence of water and less consolidated material. Besides, the modification of the crust by thinning process may have change the composition of the lower crust in the region (by lateral flow of lower crust for example). Hereafter, whenever it is possible, we try to discriminate between those two possible sources for the variation in Vp/Vs.

We can first observe that Vp/Vs ratio is increasing northward for the eastern part of the network (from S09 to S07, Fig. 10). It is correlated with a rather uniform crustal thickness (about 28 km). The low Vp/Vs value found beneath S09 (Mirbat, $\kappa = 1.67$) could be associated with the high silica content of the basement and the lack of sedimentary cover. The composition of the Precambrian basement (Gneiss and granodiorites) leads for a Vp/Vs ratio of around 1.72 (Chrisensen 1996), but felsic dykes intrusion and high thinning of the crust could have led to a more felsic composition of the crust and to a smaller value of Poisson's ratio. The Vp/Vs ratio increases then as the sedimentary cover appears in S08 (Tawin Atair) and S07 (Jibjaat). For the rest of the stations, the Vp/Vs ratio is either near 1.76 (S03, S04, S10 and S11) or 1.88 (S01, S02, S05 and S06). Their organization doesn't seem to follow a simple geographic classification (Fig. 9). The high value for S01 (Salalah, 1.86) could be related to the presence of post- and syn-rift sediment deposits within the basin (average ratio of 1.88 for limestone after Mavko *et al.* 1998). We observe a sharp jump in the Vp/Vs ratio between S02 (Ghado) and S03 (Queiroon) that echoes with the sudden deepening of the Moho at the same location (Fig. 10). Either the low value for S03 is coming from a change in the sediment thickness, or a change in the crust composition (that becomes more felsic beneath S03). S11 is associated with normal value of Vp/Vs ratio, intermediate between S09 and S01. It is representative from an area that presents small amount of sediment, yet enough to increase the Vp/Vs ratio compared with the basement related value (S09). The variation recorded for Vp/Vs ratio for S04, S10 ($\sim$1.76) and S05 and S06 ($\sim$1.81) is more difficult to explain. All these stations lay on pre-rift sediment cover which thickness is unlikely to change in few tens of kilometres. We then believe the changes in Vp/Vs ratio is due to a modification of the crustal composition. However, we can hardly go further in our interpretations.

8 CONCLUSION

We have presented and analysed receiver functions at 11 broad-band stations in the Oman southern coastline, in the Dhofar region. The results of this study lead to crustal thickness and Poisson's ratio estimations for the northern continental margin of the eastern Gulf of Aden.

We highlight a narrow zone of crustal thinning by about 10 km over a 30 km horizontal distance in the North South direction along the northern margin of the rift of Aden. An important and sharp change is occurring between station S02 and S03, where both an increase in the Moho depth (+6 km in 13 km) and a decrease of the Vp/Vs ratio (-0.11) are observed. The crustal thickness variations can be related to the extension during the break-up process. The deformation seems to have occurred in specific areas, not in a homogeneous way. We report extension concentrated beneath the first known syn-rift block. In the northern limit of our network (station S06, Thumrait), we observe a crust thinner than generally admitted for the Arabian platform. The margin could be more extended than what we previously expected from geological observations (no fault outcrops). The stations outside the main onshore-rifted basin (S07, S08 and S09) show no NS crustal thickness change and the thinner crust we observe is located at the far western end of the network, in the deformed area of the Ashawq basin (S11). Due to the N110°E striking direction of the Oligocene basins, it is possible that the maximum crustal thinning is happening offshore for the eastern part of the network. Only from the section we have onland, we can deduce a lower bound for the stretching factor β ranging from 1.38 to 1.54, assuming an initial thickness of 36–40 km for the crust, respectively.

We interpret the Vp/Vs ratio variation to be due to both sedimentary loading and modification within the crustal composition from felsic to normal. Even if we can hardly discriminate between those two sources, we could propose that the intensive thinning that occurred during the break-up process has strongly affected the crust composition. We observe three maximum Vp/Vs ratio changes. One is coincident with the highest crustal thinning in this region (between S02, Ghado and S03, Queiroon). The second is located in the eastern part of the network, where a change in the sediment thickness is likely to happen (S09, Mirbat and S07, Jibjaat). The last one spreads over the northern stations and seems to be more likely related to a crustal composition. For some stations of the network, a mid-crustal discontinuity can be evidenced. Extra processing of the signal is needed since we believe the pick of the receiver function to be a multiple and not the direct *P* to *S* conversion at this interface. For most of the case, we faithfully relate it to the sediment–basement boundary. Yet, it could also be the signature of some graben faults (particularly for S03-Queiroon station), and we need further investigations and additional information (geological and geophysical) to properly define this interface and related it to a structure of the crust in this region.

ACKNOWLEDGMENTS

This work was funded by GDRMarges and with the material of SEIS-UK. CT is grateful to the crustal group of Geophysics department of Stanford where the computing tools for the inversion were developed, and to S. Klemperer for their fruitful discussions about the nature of the crust. We are grateful to S. Chevrot for his help with the bootstrap algorithm and to J. Vergne and G. Stuart for their advices about the receiver function analysis. Many thanks to P. Denton and A. Brisbourne for their valuable help concerning the broad-band instruments, the data processing and archiving. The data were collected during field trips, where L. Labrousse, C. Brunet, C. Petit, V. Famin, S. Tabook, S. Hamdeen helped us a lot. This work benefits from the support of Dr. Hilal Mohammed Al-Azri, Sami Zubedi and Said Bin Monshir Balahaf from the Omani directorate of minerals. We thank the Regional Service, Housing Department, Forest Department and Social Development of Salalah for their authorizations to deploy the stations in Dhofar area. We thank also the Earthquake Monitoring Center of Sultan Qaboos University and Dr Issa El Hussein, Khalfan Al Toubi for his help and Adil Rabia Jaman from MOG. We are very grateful to two anonymous reviewers for their constructive remarks that help improve the manuscript. All the figures were prepared using the General Mapping Tool (Wessel & Smith 1991). The data processing and pointing were made with SAC2000 (http://www.llnl.gov/sac/). The iterative deconvolution was processing using C. Ammon's code (http://eqseis.geosc.psu.edu/∼cammon). This work was supported by NERC grant NE/C514031 and an equipment loan from the UK Geophysical Equipment Facility. GDRMarges Contribution N°2171.

REFERENCES

Al-Amri, A., 1998. The crustal structure of the Western Arabian platform from the spectral analysis of long-period P-wave amplitude ratios, *Tectonophys.,* **290,** 271–283.

Al-Amri, A., 1999. The crustal and upper-mantle structure of the interior Arabian platform, *Geophys. J. Int.,* **136,** 421–430.

Al-Damegh, K., Sandvol, E. & Barazangi, M., 2005. Crustal structure of the Arabian plate: New constraints from the analysis of teleseismic receiver functions, *Earth planet. Sci. Lett.,* **231,** 177–196.

Al-Lazki, A., Seber, D., Sandvol, E. & Barazangi, M., 2002. A crustal transect across the Oman Mountains on the eastern margin of Arabia, *GeoArabia,* **7,** 47–78.

Ammon, C., Randall, G. & Zandt, G., 1990. On the non-uniqueness of receiver function inversions, *J. geophys. Res.,* **95,** 15 303–15 318.

Bellahsen, N., Fournier, M., d'Acremont, E., Leroy, S. & Daniel, J.M., 2006. Fault reactivation and rift localization: the Northeastern Gulf of Aden margin, *Tectonics,* **25,** TC1007, doi:10.1029/2004TC001626.

Buck, W.R., 2004. Consequences of athenospheric variability on continental rifting, in *Rheology and Deformation of the Lithosphere at Continental Margins*, pp. 1–30, eds Karner, G.D., Taylor, B., Driscoll, N. & Kohlstedt, D., Columbia University Press, New York.

Chevrot, S., van der Hilst, R., 2000. The Poisson ratio of the Australian crust: geological and geophysical implications, *Earth planet. Sci. Lett.,* **183,** 121–132.

Christensen, N., 1996. Poisson's ratio and crustal seismology, *J. geophys. Res.,* **101,** 3139–3156.

Christensen, N. & Mooney, W., 1995. Seismic velocity structure and composition of the continental crust: A global view, *J. geophys. Res.,* **100,** 9761–9788.

Cochran, J.R., 1981. The Gulf of Aden: structure and evolution of a young ocean basin and continental margin, *J. geophys. Res.,* **86,** 263–287.

Courtillot, V., Jaupart, C., Manighetti, I., Tapponnier, P. & Besse, J., 1999. On causal linksbetween flood basalts and continental break-up, *Earth planet. Sci. Lett.,* **166,** 177–195.

d'Acremont, E., Leroy, S., Beslier, M.-O., Bellahsen, N., Fournier, M., Robin, C., Maia, M. & Gente, P., 2005. Structure and evolution of the eastern Gulf of Aden conjugate margins from seismic reflection data, *Geophys. J. Int.,* **160,** 869–890.

d'Acremont, E., Leroy, S., Maia, M., Patriat, P., Beslier, M-O., Bellahsen, N., Fournier, M. & Gente, P., 2006. Structure and evolution of the eastern Gulf of Aden: insights from magnetic and gravity data (MD117/Encens-Sheba cruise), *Geophys. J. Int.,* **165,** 786–803.

Ebinger, C., Yemane, T., Woldegabriel, G., Aronson, J. & Walter, R., 1993. Late Eocene-Recent volcanism and faulting in the southern main Ethiopian Rift, *J. Geol. Soc.,* **150,** 99–108.

Efron, B. & Tibshirani, R., 1991. Statistical data analysis in the computer age, *Science,* **253,** 390–395.

Endrun, B., Ceranna, L., Meier, T., Bohnhoff, M. & Harjes, H.-P., 2005. Modelling the influence of Moho topography on receiver functions: A case study from the central Hellenic subduction zone, *Geophys. Res. Lett.,* **32,** L12311, doi:10.1029/2005GL023066.

Fournier, M., Patriat, P. & Leroy, S., 2001. Reappraisal of the India-Arabia-Somalia triple junction kinematics, *Earth planet. Sci. Lett.,* **189,** 103–114.

Frederiksen, S. & Braun, J., 2001. Numerical modelling of strain localisation during extension of the continental lithosphere *Earth planet. Sci. Lett.,* **188,** 241–251.

Hébert, H., Deplus, C., Huchon, P., Khanbari, K. & Audin, L., 2001. Lithospheric structure of a nascent spreading ridge inferred from gravity data: the western Gulf of Aden, *J. geophys. Res.,* **106,** 26 345–26 363.

Huchon, P. & Khanbari, K., 2003. Syn-rift stress field history of the northern Gulf of Aden margin, Yemen, *Tectonophysics,* **364,** 147–166.

Jestin, F., Huchon, P. & Gaulier, J.-M., 1994. The Somalia plate and the East African rift system: present-day kinematics, *Geophys. J. Int.,* **116,** 637–654.

Jones, C. & Phinney, R., 1998. Seismic structure of the lithosphere from teleseismic converted arrivals observed at small arrays in the southern Sierra Nevada and vicinity, California, *J. geophys. Res.,* **103,** 10 065–10 090.

Julià, J. & Mejıa, J., 2004. Thickness and V_p/V_s ratio variation in the Iberian Crust, *Geophys. J. Int.,* **156,** 59–72.

Jung, S.J.A., Davies, G.R., Ganssen, G. & Kroon, D., 2002. Decadal-centennial scale monsoon variations in the Arabian Sea during the Early Holocene, *Geochem., Geophys., Geosyst.*, 1–1.

Kieffer, B. *et al.*, 2004. Flood and shield basalts from Ethiopia: Magmas from the African superswell, *J. Petrol.,* **45,** 793–834.

Langston, C.A., 1977. The effect of planar dipping structure on source and receiver responses for constant ray parameter, *Seism. Soc. Am. Bull.,* **67,** 1029–1050.

Langston, C.A., 1979. Structure under Mount Rainier, Washington, inferred from teleseismic body waves, *J. geophys. Res.,* **84,** 4749–4762.

Latorre, D., Virieux, J., Monfret, T., Monteiller, V., Vanorio, T., Got, J.-L. & Lyon-Caen, H., 2004. A new seismic tomography of Aigion area (Gulf of Corinth, Greece) from the 1991 data set, *Geophys. J. Int.,* **159,** 1013–1031.

Lepvrier, C., Fournier, M., Bérard, T. & Roger, J., 2002. Cenozoic extension in coastal Dhofar (southern Oman): implications on the oblique rifting of the Gulf of Aden, *Tectonophysics,* **357,** 279–293.

Leroy, S. *et al.*, 2004. From rifting to spreading in the eastern Gulf of Aden: a geophysical survey of a young oceanic basin from margin to margin, *TerraNova,* **16,** 185–192.

Leroy, S. *et al.*, 2006. The Encens project: Integrated onshore-offshore study of the northeastern margin of Aden, *GDR Marges congress*, March 2006, Paris, France.

Ligorria, J.P. & Ammon, C.J., 1999. Iterative deconvolution of teleseismic seismograms and receiver function estimation, *Bull. seism. Soc. Am.,* **89,** 1395–1400.

Mavko, G., Mukerji, T. & Dvorkin, J., 1998. *The Rock Physics Handbook: Tools for Seismic Analysis in Porous Media*, Cambridge Univ. Press, Cambridge, UK.

Mooney, W.D., Gettings, M.E., Blank, H.R. & Healy, J., 1985. Saudi Arabian seismic deep refraction profile, a travel time interpretation for crustal and upper mantle structure, *Tectonophysics,* **111,** 173–246.

Platel, J.P. & Roger, J., 1989. Evolution godynamique du Dhofar (Sultanat d'Oman) pendant le Cretace et le Tertiaire en relation avec l'ouverture du golfe d'Aden, *Bull. Soc. geol. France,* **2,** 253–263.

Rodgers, A., Walter, W., Mellors, R., Al-Amri, A. & Zhang, Y., 1999. Lithospheric structure of the Arabian Shield and Platform from complete regional waveform modelling and surface wave group velocities, *Geophys. J. Int.,* **138,** 871–878.

Roger, J., Platel, J.P., Cavelier, C. & Bourdillon de Grisac, C., 1989. Donnes nouvelles sur la stratigraphie et l'histoire gologique du Dhofar (Sultanat d'Oman), *Bull. Soc. gol. France,* **2,** 265–277.

Sandvol, E., Seber, D., Barazangi, M., Vernon, F., Mellors, R. & Al-Amri, A., 1998. Lithospheric seismic velocity discontinuities beneath the Arabian Shield, *Geophys. Res. Lett.,* **25,** 2873–2876.

Tard, F., Masse, P., Walgenwitz, F. & Gruneisen, P., 1991. The volcanic passive margin in the vicinity of Aden, Yemen, *Bull. Cent. Rech. Explor. Prod.,* **15,** 1–9.

Ukstins, I., Renne, P., Wolfenden, E., Baker, J., Ayalew, D. & Menzies M., 2002. Matching conjugate volcanic rifted margins:^{40}Ar/^{39}Ar chronostratigraphy of pre- and syn-rift bimodal flood volcanism in Ethiopia and Yemen, *Earth planet. Sci. Lett.,* **198,** 289–306.

van der Meijde, M., van der Lee, S. & Giardini, D., 2003. Crustal structure beneath broad-band seismic stations in the Mediterranean region, *Geophys. J. Int.,* **152,** 729–739.

Vanorio, T., Virieux, J., Capuano, P. & Russo, G., 2005. Three-dimensional seismic tomography from *P* wave and *S* wave microearthquake travel times and rock physics characterization of the Campi Flegrei Caldera, *J. geophys. Res.,* **110,** B03201, doi:10.1029/2004JB003102.

Vergne, J., Wittlinger, G., Hui, Q., Tapponnier, P., Poupinet, G., Mei, J., Herquel, G. & Paul, A., 2002. Seismic evidence for stepwise thickening of the crust across the NE Tibetan Plateau, *Earth planet. Sci. Lett.,* **203,** 25–33.

Wessel, P. & Smith, W.H.F., 1991. Free software helps map and display data, *EOS Trans. Am. Geophys. Un.,* **72,** 445–446.

Wolfenden, E., Ebinger, C., Yirgu, G., Renne, P. & Kelley, S., 2005. Evolution of a volcanic rifted margin: Southern Red Sea, Ethiopia, *BSA Bull.,* **117,** 846–864. doi:10.1130/B25516.1.

Zandt, G. & Ammon, C., 1995. Continental crust composition constrained by measurements of crustal Poisson's ratio, *Nature,* **374,** 152–154.

Zandt, G., Myers, S. & Wallace, T., 1995. Crust and mantle structure across the Basin and Range-Colorado Plateau boundary at 37°N latitude and implications for Cenozoic extensional mechanism, *J. geophys. Res.,* **100,** 10 529–10 548.

Zhu, L., 2000. Crustal structure across the San Andreas Fault, Southern California from teleseismic converted waves, *Earth planet. Sci. Lett.,* **179,** 183–190.

Zhu, L. & Kanamori, H., 2000. Moho depth variation in southern California from teleseismic receiver functions, *J. geophys. Res.,* **105,** 2969–2980.